The Astrophysical Journal, 723:218–228, 2010 November 1 doi:10.1088/0004-637X/723/1/218

A COMPREHENSIVE SURVEY OF HYDROGEN CHLORIDE IN THE GALAXY

Ruisheng Peng[1], Hiroshige Yoshida[1], Richard A. Chamberlin[1], Thomas G. Phillips[2], Dariusz C. Lis[2], and Maryvonne Gerin[3]
[1] Caltech Submillimeter Observatory, 111 Nowelo Street, Hilo, HI 96720, USA; peng@submm.caltech.edu, hiro@submm.caltech.edu, cham@astro.caltech.edu
[2] Division of Physics, Mathematics, and Astronomy, 320-47, California Institute of Technology, Pasadena, CA 91125, USA; tgp@submm.caltech.edu, dcl@submm.caltech.edu
[3] LERMA-LRA, CNRS, Observatoire de Paris and Ecole Normale Sup'erieure, 24 Rue Lhomond, F 75231 Paris Cedex 05, France; gerin@lra.ens.fr
Received 2010 June 18; accepted 2010 August 23; published 2010 October 8

ABSTRACT

We report new observations of the fundamental $J = 1$–0 transition of HCl (at 625.918 GHz) toward a sample of 27 galactic star-forming regions, molecular clouds, and evolved stars, carried out using the Caltech Submillimeter Observatory. Fourteen sources in the sample are also observed in the corresponding $H^{37}Cl$ $J = 1$–0 transition (at 624.978 GHz). We have obtained clear detections in all but four of the targets, often in emission. Absorptions against bright background continuum sources are also seen in nine cases, usually involving a delicate balance between emission and absorption features. From RADEX modeling, we derive gas densities and HCl column densities for sources with HCl emission. HCl is found in a wide range of environments, with gas densities ranging from 10^5 to 10^7 cm^{-3}. The HCl abundance relative to H_2 is in the range of (3–30) $\times 10^{-10}$. Comparing with the chlorine abundance in the solar neighborhood, this corresponds to a chlorine depletion factor of up to ∼400, assuming that HCl accounts for one-third of the total chlorine in the gas phase. The $[^{35}Cl]/[^{37}Cl]$ isotopic ratio is rather varied, from unity to ∼5, mostly lower than the terrestrial value of 3.1. Such variation is highly localized, and could be generated by the nucleosynthesis in supernovae, which predicts a ^{37}Cl deficiency in most models. The lower ratios seen in W3IRS4 and W3IRS5 likely confine the progenitors of the supernovae to stars with relatively large mass ($\gtrsim 25\,M_\odot$) and high metallicity ($Z \sim 0.02$).

Key words: ISM: abundances – ISM: molecules – submillimeter: ISM

1. INTRODUCTION

Initially of interest as a potential coolant for molecular clouds, hydrogen chloride (HCl) was first detected in the $J = 1$–0 transition at 625.918 GHz (De Lucia et al. 1971) toward IRc2 in Orion A, in emission, by Blake et al. (1985), and in absorption against dust continuum in Sgr B2, by Zmuidzinas et al. (1995), both on board the NASA Kuiper Airborne Observatory with a beam width of 2.′3. Ground-based observations at a higher spatial resolution of 12″ were carried out using the 10.4 m telescope of the Caltech Submillimeter Observatory (CSO) by Schilke et al. (1995) and Salez et al. (1996) toward OMC-1 and MonR2. Salez et al. (1996) also detected the $H^{37}Cl$ $J = 1$–0 transition toward OMC-1. These studies found the HCl abundance to be 10^{-9} to 10^{-10} relative to molecular hydrogen, indicating that chlorine is depleted by a factor of several hundred compared to its solar neighborhood abundance and that HCl is not a significant coolant of molecular clouds. Salez et al. (1996) also reported a $[^{35}Cl]/[^{37}Cl]$ isotopic ratio that is 1.3–2 times higher than the solar neighborhood value, indicating variations of the isotropic ratio in the Galactic interstellar medium.

Chemistry of chlorine and hydrogen chloride in the interstellar medium has been investigated by a number of authors (Jura 1974; Dalgarno et al. 1974; Blake et al. 1986; Schilke et al. 1995; Neufeld & Wolfire 2009), establishing a relatively simple chemical network involving less than a dozen other atomic and molecular species, as well as electrons and cosmic-ray particles, in the production and destruction of HCl. In dense molecular clouds, such a network yields, among other species, predominantly HCl, taking up about one-third of the chlorine in the gas phase (Schilke et al. 1995; Neufeld & Wolfire 2009).

HCl $J = 1$–0 transition falls on the shoulder of a relatively strong atmospheric water absorption line. Consequently, ground-based observations of HCl have been limited to the rare occasions of superb weather at high sites, such as Mauna Kea, and relatively little is known about HCl in different categories of objects, such as evolved stars, active star-forming regions, molecular clouds with no apparent star formation activity, etc. In particular, the $[^{35}Cl]/[^{37}Cl]$ isotopic ratio is of interest in different categories of objects, as variations of this ratio can be produced through nucleosynthesis in massive stars followed by mixing of the processed material into the surrounding molecular cloud (Salez et al. 1996). The chlorine isotopic ratio could thus offer insights into the evolutionary history of the molecular material.

To address these questions, we took advantage of several periods of superb weather on Mauna Kea to conduct a comprehensive survey of HCl in a sample of well-known objects. In the following sections, we first describe the observational details, then present the results and data analysis, followed by discussions and conclusions.

2. OBSERVATIONS

Observations described here were carried out on 2008 September 11, 2010 March 2, and April 7–15 with the 10.4 m CSO telescope. The 690 GHz facility heterodyne receiver was tuned to 625.918756 GHz and 624.977821 GHz, respectively, for observations of HCl $J = 1$–0 and $H^{37}Cl$ $J = 1$–0 lines. The lines fall on the shoulder of a prominent atmospheric water absorption line, therefore requiring premium weather conditions. The atmospheric opacity measured at 225 GHz was mostly 0.03–0.04, and the typical double-side-band system temperature was 2500 K. There were marginal periods on 2010 April 7–15 when atmospheric opacity was around 0.05–0.06, resulting in a typical system temperature of 6000 K. Both the FFTS and

Table 1
Source List of the Survey

Source	R.A. (J2000)	Decl. (J2000)	v_{LSR}	HCl	$H^{37}Cl$
W3IRS4	$02^h25^m30\overset{s}{.}90$	$62°06'20\overset{''}{.}29$	−42	Y	Y
W3IRS5	02 25 40.46	62 05 52.27	−39	Y	Y
W3(OH)	02 27 03.82	61 52 24.60	−44	Y	Y
OMC-1	05 35 14.18	−05 22 30.55	8	Y	Y
OMC-1 (0, −60)	05 35 14.18	−05 23 30.55	8	Y	Y
OMC-1 (0, −100)	05 35 14.18	−05 24 12.55	8	Y	Y
Orion Bar	05 35 23.99	−05 24 59.97	9	Y	N
MonR2	06 07 46.19	−06 23 08.30	10.5	Y	Y
IC443G1	06 16 43.44	22 32 33.50	−5	Y	N
AFGL961	06 34 37.64	04 12 43.82	15	Y	N
IRC+10216	09 47 57.30	13 16 43.05	−26	Y	Y
CIT6	10 16 02.34	30 34 18.30	−2	Y	N
IRAS16293	16 32 22.91	−24 28 35.52	4	Y	Y
Sgr B2(M)	17 47 20.16	−28 23 04.97	62	Y	Y
Sgr B2(N)	17 47 19.90	−28 22 17.78	65	Y	Y
Sgr A*	17 45 40.04	−29 00 28.10	60	Y	N
G1.6−0.025	17 49 20.61	−27 34 05.46	55	Y	N
G5.89−0.39	18 00 30.43	−24 04 01.48	10	Y	Y
G8.67−0.36	18 06 18.98	−21 37 32.10	42	Y	N
G10.62−0.38	18 10 28.67	−19 55 50.08	0.4	Y	N
W43-MM2	18 47 36.70	−02 00 51.90	90	Y	N
W43-MM1	18 47 47.00	−01 54 28.00	90	Y	N
G34.26+0.15	18 53 18.58	01 14 58.41	54.6	Y	N
W49N	19 10 13.62	09 06 17.3	0.0	Y	Y
G45.12+0.13	19 13 27.84	10 53 36.6	58.0	Y	N
W51FIR2	19 23 44.17	14 30 33.4	57.0	Y	Y
DR21(OH)	20 39 00.70	42 22 46.7	−4.7	Y	Y

4 GHz AOS facility spectrometers were used in 1 GHz mode as backends.

The dish surface optimization system (Leong et al. 2006) was used to correct gravitational deformations of the telescope surface, maintaining a clean 13.″5 beam over a wide range of elevations. Temperature calibration using a hot chopper wheel yields T_A^*, the antenna temperature corrected for atmosphere and telescope hot spillover. A main beam efficiency of ∼50% measured on Jupiter and Uranus is used to convert T_A^* to T_{mb}, the main beam brightness temperature. Telescope pointing was checked on Jupiter, Mars, and Uranus, and was found to be within 4″.

Observations were conducted in the beam switching mode at a frequency of 0.523 Hz and with a chop throw of 300″. Typical integration time on each source was 300 s, resulting in an rms of ∼0.15 K at a velocity resolution of 0.31 km s^{-1}. The source selection was primarily based on its accessibility at reasonable elevations, with a secondary goal of covering a diverse collection of objects. Due to its high critical density (∼10^8 cm^{-3}), the excitation of the HCl $J = 1$–0 transition is most likely sub-thermal, and radiative excitation, in the presence of continuum emission, is likely to play an important role in the excitation of the transition. The presence of dense gas and/or continuum radiation in an object would likely yield a detection. In the end, 27 sources/positions were observed, among them were active star-forming regions, giant molecular clouds with no apparent star-forming activities, evolved stars, shocked gas in a supernova remnant (SNR), and ultra-compact H II regions. Table 1 lists observational details for all observed sources.

3. RESULTS

For sources with matching HCl and $H^{37}Cl$ $J = 1$–0 spectra, we present in Figures 1–3 HCl spectra in the left column and $H^{37}Cl$ spectra in the right column. The antenna temperature scale is kept the same for each source for easy comparison of the line intensities. The velocity scale, $V_{LSR} - V_0$, refers to the main hyperfine component; values of V_0 are denoted in each panel. Toward IRc2 in OMC-1, the HCl and $H^{37}Cl$ line profiles are blended heavily with spectral lines from other species, in the case for $H^{37}Cl$ predominantly methanol. It is not easy to untangle the blending and derive useful information from the resulting line profile. Instead we opted to observe two positions south of IRc2 with declination offsets of −60″ and −100″, respectively. The two positions correspond to local maxima in the HCl map of OMC-1 by Schilke et al. (1995). The (0, −60″) position also coincides with the CS clump LS1 (Mundy et al. 1986) and the (0, −100″) position Orion S. Figure 4 shows the HCl $J = 1$–0 spectra for the remaining sources in the sample.

3.1. Hyperfine Structure Fitting

The HCl hyperfine structure, resulting from the interaction between the electric field and chlorine nuclear spin, splits the $J = 1$–0 transition into three components, with the outer two separated by −6.35 and 8.22 km s^{-1}, respectively, from the strongest middle component for $H^{35}Cl$. For $H^{37}Cl$, the separations are −5.05 km s^{-1} and 6.45 km s^{-1}, respectively. Statistical weights for the upper level of the hyperfine transitions dictate optically thin line strength ratio of 1:3:2. In the observed sample, the three-component hyperfine pattern is clearly seen in many sources, but the components often do not conform to the optically thin ratio, indicating deviations from the optically thin limit or differences in excitation between the three components.

Under the assumption that the hyperfine components share the same excitation and kinematic characteristics, fits to the line profiles can independently provide the optical depth and excitation temperature (Kwan & Scoville 1975). Such a utility is readily available in CLASS, the spectral line data reduction package developed and maintained by IRAM. The hyperfine structure (HFS) fit in CLASS provides four parameters: $\Delta T \cdot \tau_{main}$, V_{LSR}, w the line width, and τ_{main}. τ_{main} is the total optical depth from all hyperfine components of the line, and $\Delta T = T_{ex} - T_{bg}$ is the difference between the line excitation temperature and background temperature. Table 2 lists the results of such hyperfine structure fits for sources in our sample that show the $J = 1$–0 HCl or $H^{37}Cl$ emission. Cases involving absorption are more complex, as seen in G34.26+0.15 and W43−MM1 in Figure 3, for example. They are often the result of a delicate balance between emission and absorption features. We defer the treatment and discussions for sources with absorption to a separate paper (H. Yoshida et al. 2010, in preparation).

In fitting the hyperfine profiles in T_{mb} scale, one needs to be mindful that the line emission may suffer from beam dilution when a source is smaller than the telescope beam. The uncorrected line temperatures would affect the excitation temperature and optical depth derived from HFS fit of the HCl line profile. Thermal dust emission as seen in submillimeter continuum maps provides a good measure for gas distribution in the source. We compare the size of the 350 μm dust cores to the telescope beam of 13.″5 to determine whether the HCl emission from a given source suffers appreciable beam dilution. Most of our sources in the sample are observed by Dotson et al. (2010) with the SHARP camera at the CSO, and the FWHM of the dust cores ranges from ∼30″ to ∼60″. We therefore do not consider beam dilution a significant source of error for our sample of objects in deriving the excitation temperature and optical depth for the HCl $J = 1$–0 transition. One exception

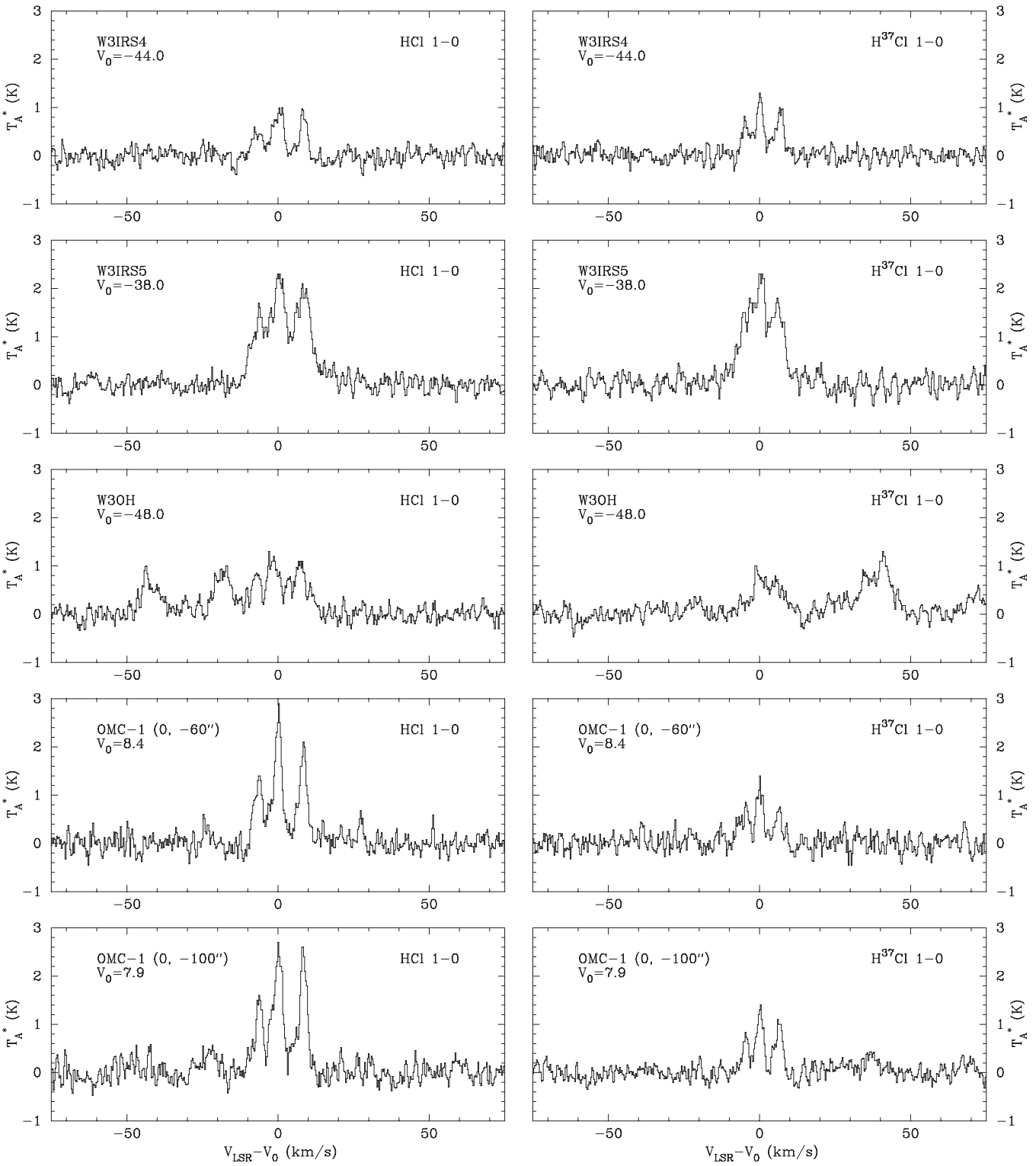

Figure 1. HCl and $H^{37}Cl$ $J = 1$–0 spectra toward W3IRS4, W3IRS5, W3(OH), and two positions in OMC-1 offset from IRc2 in declination by $-60''$and $-100''$, respectively. Velocity scale, $V_{LSR} - V_0$, refers to the main hyperfine component.

may be G5.89−0.39, where the Smithsonian Millimeter Array (SMA) continuum image at 870 μm reveals a dust core $\sim 6''$–$8''$ in size (Tang et al. 2009), implying a factor of $\sim$3 in beam dilution in the observed line temperature.

The HFS fits are sensitive to the signal-to-noise ratio (S/N) in the observed line profiles. ΔT and hence τ_{main} are not well constrained for relatively noisy line profiles. For sources with both HCl and $H^{37}Cl$ detections, one would expect the values of ΔT derived from HFS fits of the two transitions to be very close. In reality, they tend to agree within error bars, albeit rather large error bars in some cases, resulting in questionable estimates of the optical depths. We attempted to derive alternative estimates of the optical depths for both HCl and $H^{37}Cl$ lines by imposing a fixed value of $(\Delta T)^*$, a weighted average of the values obtained

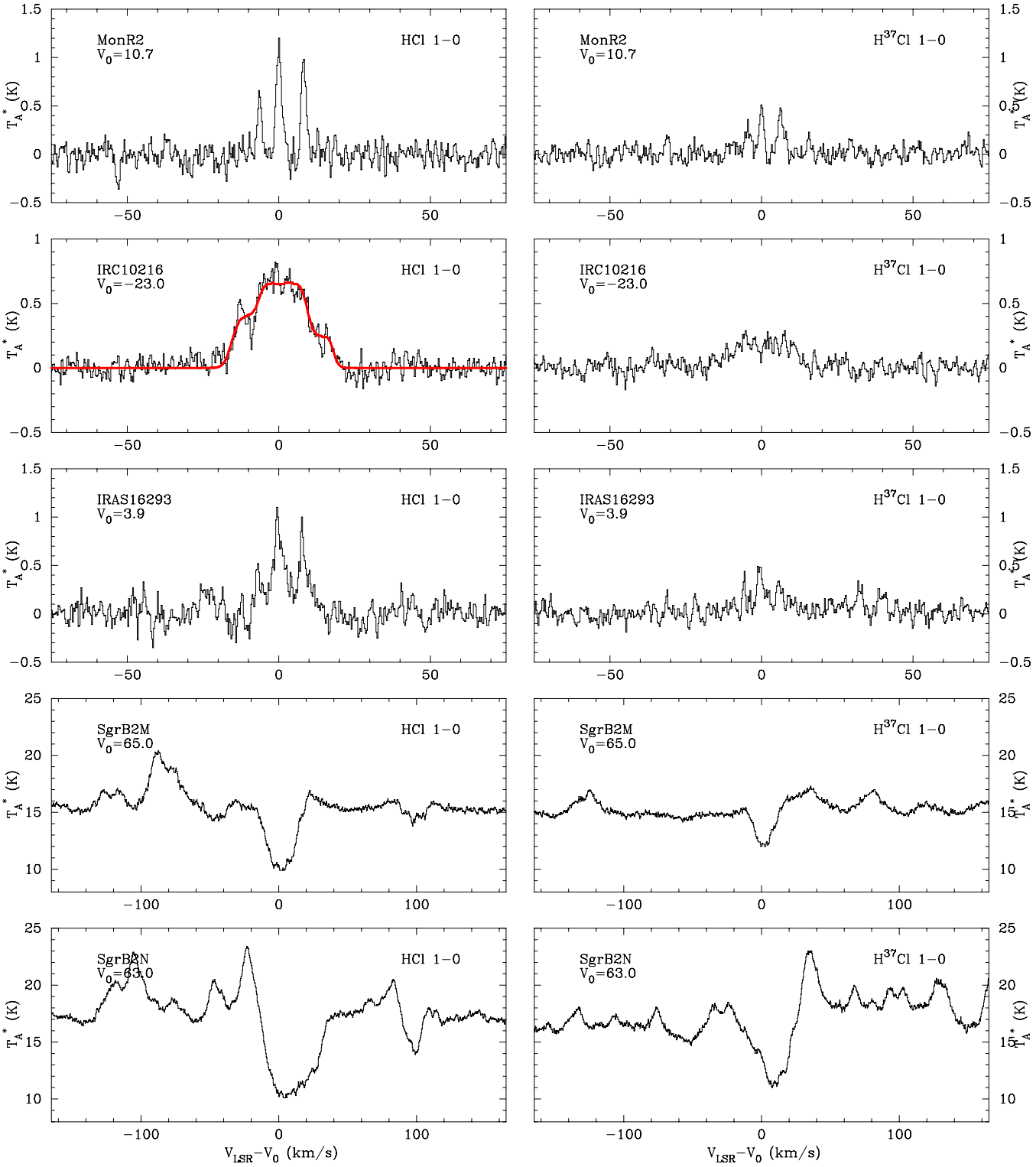

Figure 2. HCl and $H^{37}Cl$ $J = 1$–0 spectra toward MonR2, IRC+10216, IRAS16293, Sgr B2(M), and Sgr B2(N). Velocity scale, $V_{LSR} - V_0$, refers to the main hyperfine component. For sources with detectable continuum, baseline is not removed to show the continuum level.

for the two lines. Using $(\Delta T)^*$ and the T_{mb} from Gaussian fits of the three components in each profile, we derive $\tau(\mathrm{HCl})^*$ and $\tau(\mathrm{H^{37}Cl})^*$ as listed in Table 2. The error of $T_{mb}/(\Delta T)$ amplified by e^{τ} translates into the error of τ^* for each component, resulting in relatively large errors for τ^* derived from this approach when individual components are optically thick. We nonetheless consider τ^* a more reliable measure of the optical depth than that obtained directly from HFS fits. For sources that have only HCl observations, $(\Delta T)^*$ and $\tau(\mathrm{HCl})^*$ in Table 2 are from direct HFS fits. For G5.89−0.39, we also present fits corrected for the likely case of beam dilution. Compared to the uncorrected case, the differences are mostly in the line excitation temperatures, with optical depth remain largely unchanged.

IRC+10216 shows a rather distinctive line profile. It is likely the result of convolution of the hyperfine structure with a shell profile often seen in circumstellar envelopes. As an

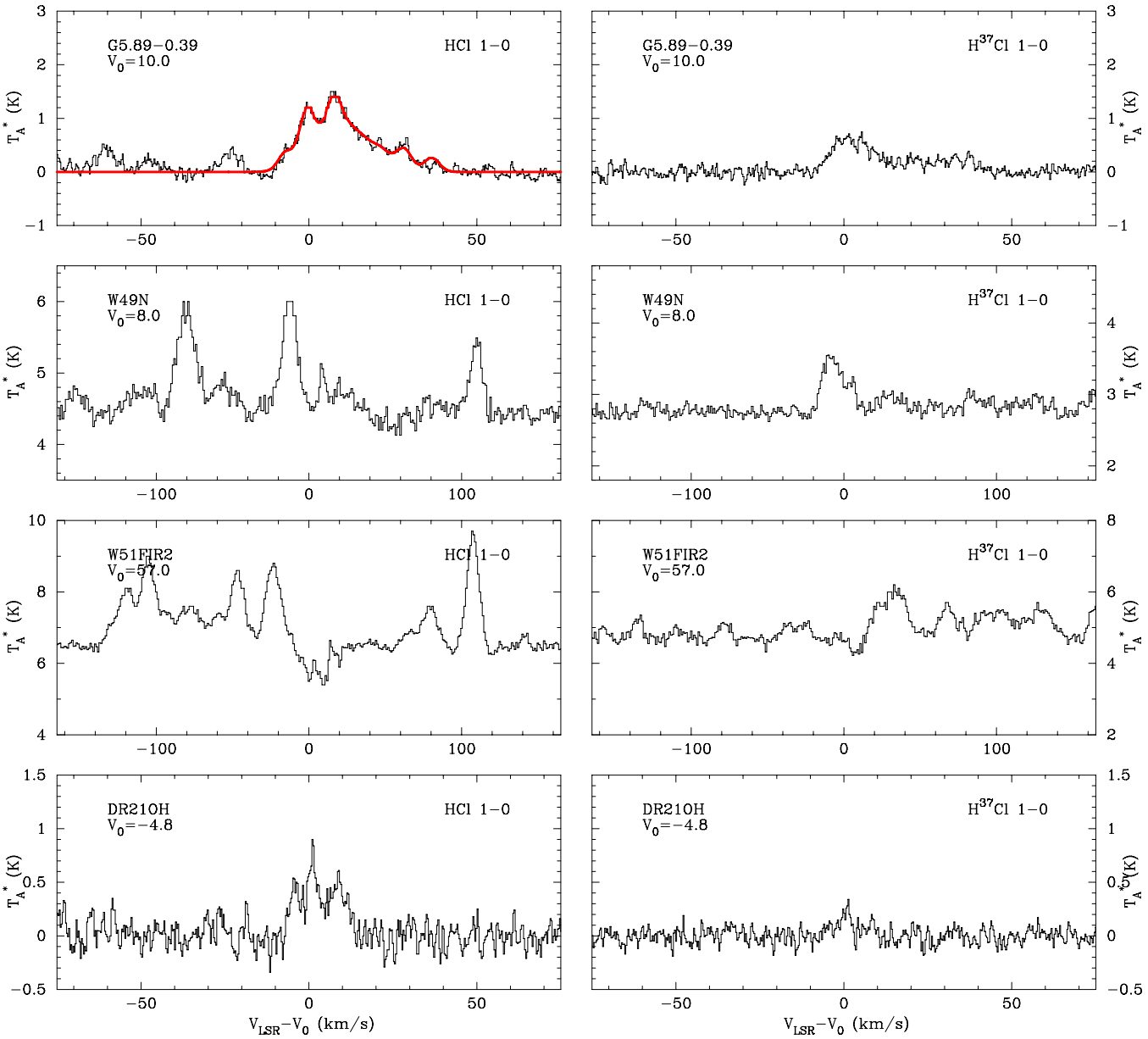

Figure 3. HCl and $H^{37}Cl$ $J = 1$–0 spectra toward G5.89−0.39, W49N, W51FIR2, and DR21(OH). Velocity scale, $V_{LSR} - V_0$, refers to the main hyperfine component. For sources with detectable continuum, baseline is not removed to show the continuum level.

approximation, we chose to fit two Gaussian profiles for IRC+10216 at local standard of rest (LSR) velocities of −17.8 km s^{-1} and −27.4 km s^{-1}, respectively, to simulate the shell profile in the hyperfine fits. As shown by the red curve in the appropriate panel in Figure 2, this approach adequately fits the line profile, yielding a solution that indicates that the HCl emission originated from a circumstellar shell with an expansion velocity of 4.8 km s^{-1}, compared to an observed terminal velocity of 14.5 km s^{-1} (see, for example, Schöier & Olofsson 2001). The $[H^{35}Cl]/[H^{37}Cl]$ isotopic ratio in the shell is likely in excess of 4 from the optical depth shown in Table 2.

CIT6 is widely regarded as similar to IRC+10216 with comparable chemical and physical characteristics, but a lower dust-to-molecular mass ratio (Zhang et al. 2009). HCl is no exception in that regard. It is clearly detected but the line is too weak to allow for a good HFS fit. Nevertheless, this observation serves as an additional proof that HCl as a species exists in detectable quantities in circumstellar shells of evolved stars. IC443G1 is a dense core in a ring of shocked material associated with SNR IC443 (van Dishoeck et al. 1993). There are tantalizing signs of HCl detection, but the line is again too weak to derive any useful parameters.

G5.89−0.39 is another interesting case with a rather distinctive line profile. Both HCl and $H^{37}Cl$ line show a pronounced red wing, indicating the presence of higher velocity components. A three-component fit, as shown by the red curve in the top left panel of Figure 3, represents an excellent match to the observed line profile. As listed in Table 2, the three components are at LSR velocities of 9.3, 17.9, and 38.3 km s^{-1}, with FWHM line widths of 4.9, 13.5, and 5.4 km s^{-1}, respectively. From the interferometric study of Hunter et al. (2008), the broad (∼13 km s^{-1}) line emission is seen in $C^{34}S$, SiO, CH_3OH, HC_3N, $C^{17}O$, and $H^{13}CO^+$ toward the dust emission source SMA-N, in the north–northeast extension of the molecular ridge that bounds the northern and western edges of the UCHII. The 9.3 km s^{-1} feature likely originates from the northwest and southwest

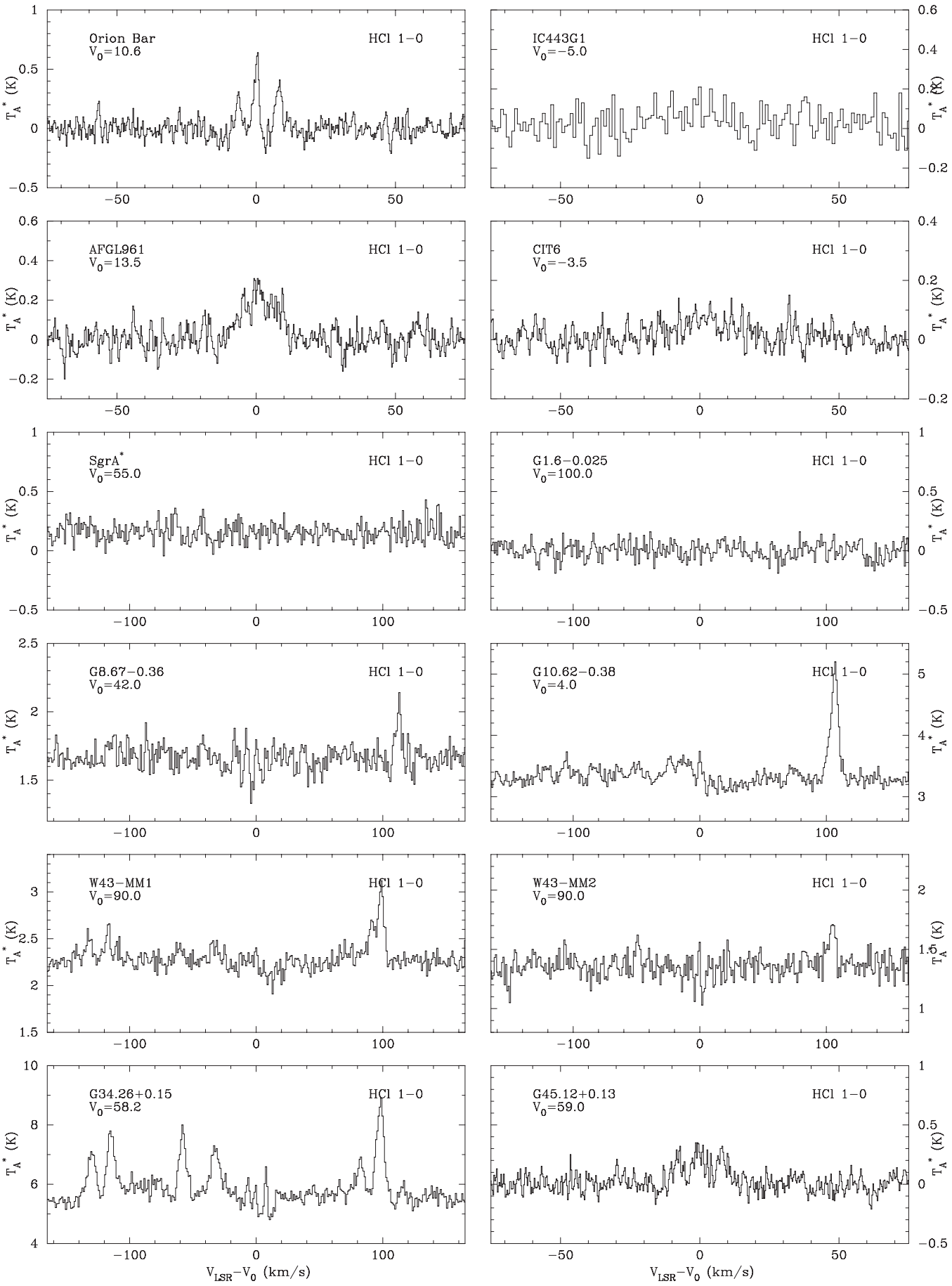

Figure 4. HCl spectra toward rest of the sources in the sample.

Table 2
Hyperfine Structure Fits for HCl and $H^{37}Cl$ Line Emission

Source	v_{LSR}	w	HCl					$H^{37}Cl$					$(\Delta T)^*$	$\tau(HCl)^*$	$\tau(H^{37}Cl)^*$
			S_1	S_2	S_3	$(\Delta T \cdot \tau)$	τ	S_1	S_2	S_3	$(\Delta T \cdot \tau)$	τ			
W3IRS4	−44.0	3.2	4.0	7.7	5.9	7.9(1.2)	3.7(1.1)	4.4	8.0	6.7	6.7(0.6)	1.8(0.6)	2.7(0.8)	2.5(2.1)	2.8(2.5)
W3IRS5	−37.9	4.8	15.7	24.9	24.3	24.6(1.9)	5.8(0.7)	12.8	22.7	17.8	16.0(0.9)	3.1(0.3)	4.6(0.4)	5.0(2.3)	3.3(1.0)
W3(OH)	−49.2	4.9	7.9	12.0	12.2	11.3(1.8)	5.3(1.2)	1.5	9.2	7.0	3.9(0.5)	0.7(0.7)	2.2(0.6)	4.9(6.9)	1.9(2.3)
OMC1 (0, −60)	8.4	3.1	9.6	17.6	13.2	15.1(1.4)	2.0(0.5)	4.9	7.6	4.4	5.4(0.7)	1.0(0.7)	7.5(0.7)	2.2(0.6)	0.7(0.2)
OMC1 (0, −100)	7.9	3.2	10.7	19.3	17.1	20.3(2.7)	3.5(0.9)	4.2	8.5	7.0	6.0(0.6)	0.7(0.6)	6.1(0.7)	3.6(1.6)	1.0(0.3)
ORIONBAR[a]	10.6	1.9	1.2	2.6	1.8	3.6(0.4)	2.3(0.6)	...	...	...	...	...	1.6(0.4)	2.3(0.6)	...
MonR2	10.7	1.7	2.3	4.8	4.0	9.0(0.6)	3.3(0.4)	1.1	2.0	2.0	4.1(0.8)	3.6(1.4)	2.5(0.5)	4.4(4.3)	1.1(0.5)
AFGL961[a]	13.4	6.5	1.3	3.4	2.3	1.1(0.1)	0.4(0.3)	...	...	...	...	...	2.8(2.5)	0.4(0.3)	...
IRC+10216	−17.8	6.4	5.2	2.8	5.5	9.6(0.1)	17.8(0.1)	0.4	0.8	1.4	0.8(0.3)	5.0(3.0)	0.54(0.01)	7.3(6.8)	0.8(0.5)
	−27.4	8.5	6.5	5.9	9.1	6.0(0.1)	6.5(0.1)	2.0	1.8	2.0	3.2(3.0)	11.6(1.5)	0.93(0.01)	3.2(0.6)	0.8(0.2)
IRAS16293	3.9	4.2	3.0	8.2	6.2	4.5(0.3)	1.1(0.4)	1.4	3.2	2.3	2.0(0.5)	0.6(0.7)	3.7(1.1)	1.1(0.3)	0.4(0.1)
G5.89−0.39[b,c]	9.3	4.9	2.7	8.0	6.0	3.5(0.7)	0.7(0.5)	1.0	5.2	3.9	2.1(0.2)	0.5(0.4)	4.6(0.4)	0.8(0.2)	0.5(0.2)
	17.8	13.5	10.3	17.0	10.3	2.8(0.2)	0.3(0.2)	3.2	5.3	2.4	2.0(0.5)	4.1(1.2)	9.4(4.6)	0.3(0.3)	0.08(0.07)
	38.3	5.4	1.7	5.3	1.7	1.6(0.2)	0.1(0.1)	0.6	2.1	0.4	0.6(0.1)	0.1(1.1)	15(8)	0.1(0.1)	0.03(0.03)
G5.89−0.39[c,d]	9.3	4.9	8.0	24.0	17.8	10.8(2.1)	0.7(0.5)	2.8	15.9	11.7	6.4(0.5)	0.5(0.4)	13.4(1.3)	0.8(0.3)	0.5(0.3)
	17.9	13.3	30.6	50.6	31.5	8.7(0.5)	0.4(0.2)	9.7	15.9	7.2	6.3(1.4)	4.3(1.2)	24(11)	0.4(0.3)	0.10(0.08)
	38.3	5.4	5.2	15.8	5.0	4.8(0.3)	0.1(0.1)	2.0	6.4	1.1	1.9(0.2)	0.1(0.8)	48(24)	0.1(0.1)	0.03(0.03)
G45.12+0.13[a]	58.5	3.8	1.8	2.8	2.5	3.1(0.7)	5.2(1.8)	...	...	...	...	...	0.6(0.2)	5.2(1.8)	...
DR21(OH)[e]	−3.6	4.7	3.4	6.9	5.6	4.4(0.4)	2.6(0.6)	0.6	1.9	0.9	0.9(0.1)	0.1(1.0)	1.7(0.2)	2.7(1.7)	0.4(0.3)

Notes. Numbers in parentheses are quoted error bars; S_1, S_2, and S_3 are integrated intensities for the $F = 1/2$–$3/2$, $5/2$–$3/2$, and $3/2$–$3/2$ components of the $J = 1$–0 transition, respectively.
[a] $(\Delta T)^*$ and $\tau(HCl)^*$ are from HFS fit of the HCl line profile.
[b] Assuming no appreciable beam dilution.
[c] $(\Delta T)^*$ for the 18.0 km s^{-1} and 38.3 km s^{-1} components are from the HCl measurements alone as the low S/N in the $H^{37}Cl$ counterparts prevent reliable HFS fits.
[d] Accounting for a likely ×3 beam dilution.
[e] $(\Delta T)^*$ is from the HCl measurement alone as the low S/N in the $H^{37}Cl$ counterparts prevent reliable HFS fit.

sections of the molecular ridge. While the origin of the 38.3 km s^{-1} feature is not immediately clear, velocity features as highly redshifted as 78 km s^{-1} and blueshifted as −61 km s^{-1}, mostly from various masers, were quoted by these authors in establishing a north–south bipolar outflow. In deriving the alternate optical depth of these velocity components in Table 2, we opted to use the ΔT from the HCl HFS fits for the 17.9 km s^{-1} and 38.3 km s^{-1} components due to their low S/N ratio in the $H^{37}Cl$ line profile. From the derived τ^* in Table 2, the [HCl]/[$H^{37}Cl$] isotopic ratio in the source is most likely around 2, though the broad emission feature may have a higher ratio on the order of 3–4.

Sgr A*, the dynamical center of the Galaxy, yields no HCl detection to an rms level of 0.1 K at a resolution of 0.31 km s^{-1}. Similarly, G1.6−0.025, a giant molecular cloud in the Galactic center region with no apparent sign of star formation, also yields a non-detection. Sgr B2(M) and Sgr B2(N), on the other hand, show broad strong absorption at both HCl and $H^{35}Cl$ $J = 1$–0 transitions.

From Table 2, it is clear that the [$H^{35}Cl$]/[$H^{37}Cl$] isotopic ratio, based on that of the optical depth, is rather varied, from 4 and over in Mon R2, IRC+10216, and DR21(OH), to around 3 in OMC-1, W3(OH), and IRAS16293, down to around 2 in G5.89−0.39, and to nearly reaching parity in W3IRS4 and W3IRS5. In comparison, the terrestrial [^{35}Cl]/[^{37}Cl] abundance ratio is ∼3.1.

3.2. RADEX Simulations

In addition to the optical depth obtained from hyperfine structure fitting, we can derive other physical parameters from the line profiles by running large velocity gradient (LVG) simulations to fit the three HCl hyperfine components. RADEX, a computer program developed and maintained by van der Tak et al. (2007) for fast non-LTE analysis of interstellar line spectra, was used in the LVG mode to find the best combination of gas density and HCl column density that could reproduce the observed line temperatures under given gas temperature.

The molecular data file for HCl under RADEX includes the hyperfine levels of the lowest eight rotational levels, up to 839 K above ground level, with rates for radiative and collisional transitions among them. The collisional rates between HCl and H_2 are scaled from those of HCl and helium (Neufeld & Green 1994). The average Galactic background radiation field adopted in RADEX consists of the cosmic microwave background, average Galactic starlight in the solar neighborhood in ultraviolet/visible/near-infrared part of the spectrum, and single-temperature fit to the Galactic thermal dust emission for the far-infrared and submillimeter parts of the spectrum. Contributions from non-thermal radiation in the Galaxy are also included for low-frequency part of the spectrum (⩽30 GHz). This composite interstellar radiation field and any additional continuum background from user input provide radiative excitation in the RADEX formulism. For the subset of our sample where HCl emission is observed, no significant continuum is seen in any of these sources. We therefore use the default composite interstellar radiation field in RADEX simulations.

Simulations were run in off-line mode to cover a large parameter space, and relative χ^2 was sought between the observed line temperatures and the model results relative to the observed line temperature. Under the assumption that the observed HCl emission suffers no significant beam dilution, this process yields for a given gas temperature the most likely combination of gas density and HCl column density to reproduce the observed line strength of the hyperfine components. Figure 5 shows a RADEX simulation run for OMC-1 (0, −60″) with a gas temperature of 45 K. Contours are the relative χ^2 starting from

Table 3
RADEX fits for HCl and $H^{37}Cl$ Line Emission

Source	T_K	$N(H_2)$	$n(H_2)$	N(HCl)	$N(H^{37}Cl)$	X[HCl]	$X[^{35}Cl/^{37}Cl]$	R
W3IRS4	55[1]	3(23)[1]	(1–3)(6)	(6.3–9.1)(13)	(8.1–10.2)(13)	3(-10)	$0.8^{+0.3}_{-0.2}$	0.9
W3IRS5	100[1]	5(23)[1]	(8–13)(5)	(1.5–2.2)(14)	(1.3–1.8)(14)	4(-10)	$1.2^{+0.5}_{-0.4}$	1.2
W3OH	150[1]	4(23)[1]	(2–3)(5)	(1.5–2.4)(14)	(7.0–9.9)(13)	5(-10)	$2.3^{+1.2}_{-0.8}$	1.8
OMC-1(0, −60)	45[2]	7.4(22)[3]	(1–2)(7)	(5.1–6.3)(13)	(1.8–2.8)(13)	8(-10)	$2.5^{+0.9}_{-0.7}$	2.4
OMC-1(0, −100)	30[2]	7.4(22)[3]	(8–11)(6)	(1.3–1.5)(14)	(5.5–7.8)(13)	2(-9)	$2.1^{+0.5}_{-0.5}$	2.4
Orion Bar	75[4]	2.3(22)[3]	(1–3)(6)	(2.5–4.3)(13)	...	1(-9)	...	...
MonR2	70[5]	3.9(22)[5,6]	(1–3)(6)	(5.7–9.3)(13)	(2.8–3.7)(13)	2(-9)	$2.3^{+1.0}_{-0.7}$	2.2
AFGL961	20[7]	1.1(22)[8]	(7–10)(6)	(1.9–2.5)(13)	...	2(-9)	...	...
IRC+10216	50[9]	7(20)[10]	(5–30)(4)	(5.7–8.8)(14)	(2.6–3.0)(14)	1(-6)	$2.6^{+0.8}_{-0.7}$	4.2
IRAS16293	80[11]	2(23)[11]	(1–4)(6)	(3.0–4.7)(13)	(1.3–2.4)(13)	2(-10)	$2.1^{+1.6}_{-0.8}$	2.5
G5.89-0.39[a]	70[12]	3.1(22)[12]	(1–5)(6)	(5.4–7.5)(13)	(2.8–3.3)(13)	2(-9)	$2.1^{+0.6}_{-0.5}$	2.6
G5.89-0.39[b]	70[12]	3.1(22)[12]	(3–13)(6)	(7.4–10.1)(13)	(3.2–3.9)(13)	3(-9)	$2.5^{+0.7}_{-0.6}$	2.6
G45.12+0.13	25[13]	1.2(23)[13]	(9-12)(5)	(1.5–2.0)(14)	...	1(-9)	...	...
DR21(OH)	40[14]	3(23)[14]	(1–3)(6)	(7.1–11.3)(13)	(1.2–2.5)(13)	3(-10)	$5.0^{+4.1}_{-2.1}$	4.7

Notes. The numbers in the rightmost parentheses are exponents to the power of 10; R is the integrated intensity ratio of the HCl and $H^{37}Cl$ $J = 1$–0 transition.
[a] Assuming no appreciable beam dilution.
[b] Accounting for a likely ×3 beam dilution.
References. (1) Helmich et al. 1994; (2) Bergin et al. 1994; (3) Goldsmith et al. 1997; (4) Lis et al. 1998; (5) Choi et al. 2000; (6) Tafalla et al. 1997; (7) Williams et al. 2009; (8) Schneider et al. 1998; (9) Schöier & Olofsson 2000; (10) Cernicharo et al. 2000; (11) van Dishoeck et al. 1995; (12) Thompson & Macdonald 1999; (13) Hofner et al. 1997; (14) Chandler et al. 1993

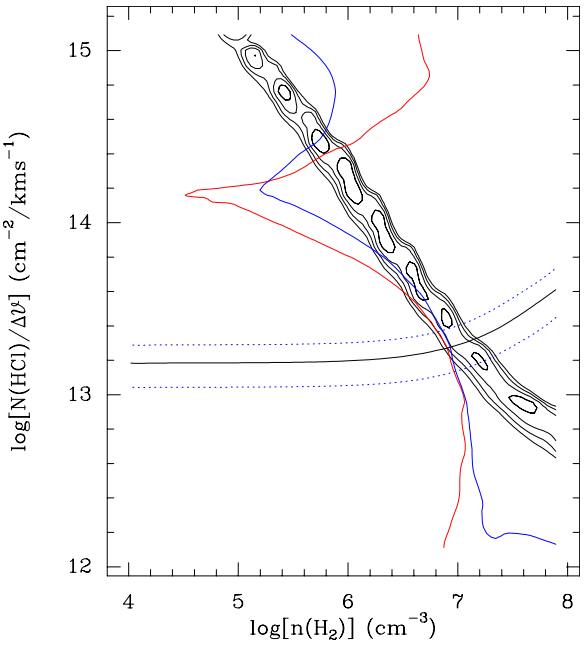

Figure 5. RADEX simulation run for OMC-1 (0, −60″) with a fixed gas temperature of 45 K. Contours are the relative χ^2 between the observed and modeled line temperatures, starting from 0.5 with a step of −0.1; blue and red curves mark the hyperfine component ratios under optically thin limit (3 between $F = 5/2$–$3/2$ and $F = 1/2$–$3/2$ transitions in blue, 1.5 between $F = 5/2$–$3/2$ and F=3/2–3/2 transitions in red). The smooth solid line and two dotted lines mark the observed optical depth of the HCl line and its $\pm 1\sigma$ error bars.

0.5 with a step of −0.1; blue and red curves mark the hyperfine component ratios under optically thin limit (3 between $F = 5/2$–$3/2$ and $F = 1/2$–$3/2$ transitions in blue, 1.5 between $F = 5/2$–$3/2$ and $F = 3/2$–$3/2$ transitions in red). The solid smooth line denotes the observed optical depth for the HCl line and the two dotted lines its $\pm 1\sigma$ error bar. In cases where the quoted errors for HCl optical depth in Table 2 exceed 30%, we generally use 30% to set the error bar for the optical depth. The cross section between the χ^2 contours and the optical depth curves clearly confines gas density and HCl column density in an often tight range.

Table 3 lists for each source the adopted gas temperature and H_2 column density, the gas density and HCl column density derived from RADEX simulations, as well as the HCl abundance. Since there is no molecular data file for $H^{37}Cl$ to use under RADEX, we treat it the same as HCl and fit the $H^{37}Cl$ line temperatures with the same procedure. Instead of confining the ranges of gas density and $H^{37}Cl$ column density with the relative χ^2 contours and optical depth curves, we use gas density ranges found in the corresponding HCl simulation of the source in place of optical depth curves, ensuring that both HCl and $H^{37}Cl$ emission originated from the same region. The resulting $H^{37}Cl$ column density is listed in Table 3 for sources with observed $H^{37}Cl$ line emission. For these sources we also list the $^{35}Cl/^{37}Cl$ abundance ratio $X[^{35}Cl/^{37}Cl]$ as measured by the ratio of HCl and $H^{37}Cl$ column densities. Cernicharo et al. (2010a) recently suggested that the integrated intensity ratio be a good gauge for HCl and $H^{37}Cl$ isotopic ratio. We listed in Table 3 the integrated intensity ratio, R, which appears to be in good agreement with our derived chlorine isotopic ratio.

4. DISCUSSION

4.1. Where to Look for HCl Emission?

From Table 3 it is clear that HCl emission is associated with warm dense gas with a density on the order of 10^6 cm^{-3}. Given a critical density of a few $\times 10^8$ cm^{-3}, molecular excitation is mostly sub-thermal, dominated by radiative processes rather than collisions with H_2. Sources with strong continuum and/or dust emission would likely yield strong HCl line emission.

The derived gas densities for the two OMC-1 cores appear to be somewhat higher than $\sim 5 \times 10^6$ established by the multi-transitional study of HC_3N (Bergin et al. 1996). This may

indicate that the gas temperatures adopted for these cores for the RADEX simulations should have been higher. Another factor may be the average Galactic background radiation field used in RADEX for radiative excitation. As HCl transitions are shortward of ∼480 μm in wavelength, radiation from warm dust would contribute significantly to the molecular excitation. Including local warm dust in the radiation field for RADEX simulation would produce a more precise picture of the gas where HCl emission originates.

The non-detection toward Sgr A* likely reflects a genuine lack of HCl molecules in the circumstellar disk surrounding Sgr A*. Latvakoski et al. (1999) show a warm dust ring ∼80″ in size, as well as the "minispiral" within the ring. The dust ring coincides with a molecular ring with sharp inner edges seen in HCN (Güsten et al. 1987). With our 13.″5 telescope beam, we are clearly probing the molecular cavity around Sgr A*. Using an FWHM (15 km s^{-1}) and the integrated line intensity of the C^{18}O J = 2–1 line we obtain toward Sgr A*, and assuming LTE at 250 K (Bradford et al. 2005), we derive a C^{18}O column density of 9×10^{15} cm^{-2} and an H_2 column density of 5×10^{22} with a C^{18}O abundance of 1.7×10^{-7} (Goldsmith et al. 1997). A upper limit of 4×10^{12} cm^{-2} is derived for the HCl column density by RADEX simulations for an HCl line of 0.1 K with an FWHM of 15 km s^{-1} (from the C^{18}O spectrum), yielding an upper limit of 8×10^{-11} for HCl abundance relative to H_2 toward Sgr A*, markedly lower than those listed in Table 3.

The non-detection in G1.6−0.025 is intriguing. The source is a giant molecular cloud located in the Central Molecular Zone (CMZ) of the Galaxy, a region characterized by elevated gas temperature (typically ∼70 K), higher gas density ($\geqslant10^4$ cm^{-3}), and highly supersonic internal velocity dispersion (∼15–50 km s^{-1}; Morris & Serabyn 1996). Dense cloud cores are seen in various molecular tracers (Gardner & Whiteoak 1981; Gardner & Boes 1987; Whiteoak & Peng 1989; Kuiper et al. 1993; Menten et al. 2009), yet there is little sign of apparent star-forming activity in the cloud. For the extended 50 km s^{-1} cloud of G1.6−0.025, we derive a C^{18}O column density of 2×10^{15} from the C^{18}O J = 2-1 spectrum taken at the CSO, assuming LTE at a gas temperature of 30 K (Menten et al. 2009). Again with a C^{18}O abundance of 1.7×10^{-7}, the cloud has an H_2 column density of 1×10^{22} cm^{-2}. Similar to Sgr A*, we obtain an upper limit of 7×10^{12} for HCl column density by modeling an HCl line of 0.1 K with 28 km s^{-1} in line width, yielding an HCl abundance of $\lesssim 7 \times 10^{-10}$ relative to H_2. It would look as though the HCl non-detection in the 50 km s^{-1} cloud of G1.6−0.025 is the result of a combination of relatively low H_2 column density and HCl abundance.

It would be interesting to see if other clouds in CMZ have similarly low HCl abundance seen in Sgr A* and the 50 km s^{-1} cloud of G1.6−0.025. A prime target would be M-0.02-0.07, the so-called 20 km s^{-1} cloud ∼2′ northeast of Sgr A*. A common trait among the three clouds is the likely interaction with an SNR (Menten et al. 2009). It is not clear though how such interaction would lead to relatively low production of HCl.

In the same vein, IC443G1 may represent another case where chemistry plays an important role in the detection of HCl. Clump G1 is a dense core in a ring of shocked material associated with SNR IC443 (van Dishoeck et al. 1993). It has a relatively rich chemistry compared to the pre-shock gas, but lacks many of the more complicated molecular species, such as methanol. These authors argued that such deficiency could be the result of the disruption of the chemical network brought on by the infusion of atomic hydrogen to the shocked gas by repeated shocks, as atomic hydrogen rapidly destroys many of the intermediate molecules in the reaction network. To derive an estimate of HCl column density from the low signal-to-noise detection, we use RADEX simulation to reproduce an HCl line of 0.2 K with an FWHM of 10 km s^{-1} (van Dishoeck et al. 1993). The resulting HCl column density of 3×10^{12} cm^{-2}, when compared to an H_2 column density of 1×10^{22} (van Dishoeck et al. 1993), leads to an HCl abundance of 3×10^{-10}. Again, the weak HCl line emission from IC443 Clump G1 may be the result of relatively low HCl abundance and H_2 column density. More observations of similar cores are needed to confirm that shocked gas may have a somewhat lower HCl abundance compared to other similarly dense gas in star-forming regions, PDRs, and ultra-compact H II regions.

Ultra-compact H II regions with reasonably high emission measures have proven to be a treasure trove for detecting HCl absorption (see Figure 4). Such cases typically involve a delicate balance between an emission feature and an absorption feature. Our forthcoming paper (H. Yoshida et al. 2010, in preparation) will discuss these cases.

4.2. The Case of IRC+10216

In Figure 2, we have shown that the HCl line profile for IRC+10216 could be adequately fit by two Gaussians centered at −17.8 km s^{-1} and −27.4 km s^{-1}, respectively, indicating that the HCl emission is associated with a circumstellar shell with an expansion velocity of 4.8 km s^{-1}. The HCl emission is likely from a density-enhanced shell ∼15″ from the central star as seen in H^{13}CN (Schöier et al. 2007) and SiO (Schöier et al. 2006), and modeled by Cordiner & Millar (2009). Radiation from the central star, as well as from local dust, contributes significantly to the molecular excitation. We therefore consider the HCl abundance and [^{35}Cl/^{37}Cl] abundance ratio for IRC+10216 as listed in Table 3 highly uncertain. More sophisticated modeling efforts such as Schöier & Olofsson (2001) and Wyrowski et al. (2006) are required to correctly interpret the results for IRC+10216. Cernicharo et al. (2010b) recently reported an HCl abundance of 5×10^{-8} from their Herschel SPIRE and PACS observations of IRC+10216. It may be interesting to note that we derive an upper limit of 8×10^{-8} for the HCL abundance in CIT6 by treating the low signal-to-noise detection as a 0.2 K line with 20 km s^{-1} in line width. Similar to the procedure used in Sgr A* and G1.6−0.025, the resulting HCl column density is 5×10^{12} cm^{-2}, with an adopted gas temperature of 40 K and an H_2 column density of 6.3×10^{19} cm^{-2} (Zhang et al. 2009).

4.3. $^{35}Cl/^{37}Cl$ Abundance Ratio

As listed in Table 3, the ^{35}Cl/^{37}Cl abundance ratio varies from around unity to around 3 and over. Cernicharo et al. (2000) reported an X[^{35}Cl/^{37}Cl] ratio of 3.1 ± 0.6 from line intensity ratios of NaCl, KCl, and AlCl in IRC+10216. Recent Herschel HIFI observations show an X[^{35}Cl/^{37}Cl] ratio of 2.7 in NGC6334I (Lis et al. 2010) and 2.1 ± 0.5 in W3A (Cernicharo et al. 2010b). These are comparable to the terrestrial value of ∼3.1. It is interesting to note that the ^{35}Cl/^{37}Cl abundance ratio is in good agreement with the integration line intensity ratio of the HCl and H^{37}Cl line, as predicted by the modeling efforts of Cernicharo et al. (2010a) for their *Herschel* HIFI observations of W3A.

One may argue that the low isotopic ratio observed in W3IRS4 might be the result of observing an unresolved, very optically thick source. DR21(OH), which is at a comparable distance (∼2.5 kpc versus ∼2.2 kpc for W3IRS4), with a comparable dust core size at 350 μm (Dotson et al. 2010) and HCl opacity, argues against this scenario.

Clearly, variations in HCl isotopic ratio are highly localized. Salez et al. (1996) suggested one likely origin for such variations through explosive nucleosynthesis, whereby enrichment of one isotopolog over the other, as synthesized in massive stars, is mixed into the surrounding molecular cloud through explosive processes such as supernova explosions.

Models for nucleosynthesis in Type Ia supernovae (SNe Ia; Travaglio et al. 2004 and references therein) and Type II supernovae (SNe II; Nomoto et al. 1997, 2006; Kobayashi et al. 2006) indeed show a general deficiency of ^{37}Cl in the processed material in most cases. In SNe Ia, the ^{35}Cl/^{37}Cl abundance ratios vary from 3.5 to 5.4 among models of different ignition conditions in the central white dwarf before the thermonuclear runaway (Travaglio et al. 2004). In SNe II, the elemental yields of the nucleosynthesis depend on the mass and metallicity of the progenitor as well as the explosion energy. Kobayashi et al. (2006) show that the ^{35}Cl/^{37}Cl abundance ratios produced in SNe with high explosion energy ($\gtrsim$10 E_{51} with $E_{51} \sim 10^{51}$ erg, so-called hypernovae) are typically in the range of 1.1–2.8 for varying progenitor mass and metallicity, while the ratios vary in a larger range (to as high as 18) in normal SNe (with explosion energy $\sim E_{51}$). It is interesting to note that in normal SNe II with relatively large progenitor mass ($\gtrsim$25 $M_\odot$) and metallicity ($Z \sim 0.02$), the ^{35}Cl/^{37}Cl abundance ratios are consistently below unity to as low as ∼0.5 (Kobayashi et al. 2006). Given enough mixing with the surrounding molecular clouds, these ratios could support the observed range of the ^{35}Cl/^{37}Cl abundance ratio.

W3IRS4 and possibly W3IRS5 present interesting exceptions of relative ^{37}Cl deficiency predicted in most nucleosynthesis models of SNe. This likely confines the progenitors of the SNe to be stars of relatively high mass ($\gtrsim$25 $M_\odot$) and high metallicity ($Z \sim 0.02$).

Kawabata et al. (2010) and Perets et al. (2010) recently reported the discovery of a new category of subluminous supernovae. Although the origin for such faint supernovae is still controversial, these authors reported the unusual composition in the supernovae ejecta to be rich with helium and calcium. It would be interesting to examine the nucleosynthesis yields in this class of supernovae in regard to the ^{35}Cl/^{37}Cl abundance ratios.

5. CONCLUSION

We conducted a comprehensive survey of HCl $J = 1$–0 line in the Galaxy. Of the 27 sources/positions observed, 14 show emission, 9 show absorption, 2 showed marginal detection in emission, and 2 are non-detections. Fourteen of the sources/positions were also observed in the H^{37}Cl $J = 1$–0 transition.

RADEX simulations show that HCl emission is mostly associated with warm dense gas, of order 10^6 cm^{-3}. HCl abundance is fairly uniform, in the range 10^{-10} to a few $\times 10^{-9}$, in general agreement with previous studies of OMC-1 by Schilke et al. (1995) and Salez et al. (1996). However, ^{35}Cl/^{37}Cl abundance ratios are found to vary considerably from around unity in W3IRS4 and W3IRS5 to ∼5 in DR21(OH). They are in good agreement to the integrated intensity ratios of the HCl and H^{37}Cl line as suggested by Cernicharo et al. (2010a).

The variations of the ^{35}Cl/^{37}Cl abundance ratios are found to be highly localized. They could be supported by the varying yields of nucleosynthesis of supernovae from different progenitors. The low ^{35}Cl/^{37}Cl abundance ratios seen in W3IRS4 and W3IRS5 likely confine the progenitors of the supernovae to stars of relatively high mass ($\gtrsim$25 $M_\odot$) and high metallicity ($Z \sim 0.02$).

Caltech Submillimeter Observatory (CSO) is supported through NSF grant AST-0540882.

REFERENCES

Bergin, E. A., Goldsmith, P. F., Snell, R. L., & Ungerechts, H. 1994, ApJ, 431, 674
Bergin, E. A., Snell, R. L., & Goldsmith, P. F. 1996, ApJ, 460, 343
Blake, G. A., Keene, J., & Phillips, T. G. 1985, ApJ, 295, 501
Blake, G. A., Anicich, V. G., & Huntress, W. T. 1986, ApJ, 300, 415
Bradford, C. M., Stacey, G. J., Nikola, T., Bolatto, A. D., Jackson, J. M., Savage, M. L., & Davidson, J. A. 2005, ApJ, 623, 866
Cernicharo, J., Guélin, M., & Kahane, C. 2000, A&AS, 142, 181
Cernicharo, J., et al. 2010a, A&A, 158, L115
Cernicharo, J., et al. 2010b, A&A, 158, L136
Chandler, C. J., Moore, T. J. T., Mountain, C. M., & Yamashita, T. 1993, MNRAS, 261, 694
Choi, M., Evans, N. J., Tafalla, M., & Bachiller, R. 2000, ApJ, 538, 738
Cordiner, M. A., & Millar, T. J. 2009, ApJ, 697, 68
Dalgarno, A., de Jong, T., Oppenheimer, M., & Black, J. H. 1974, ApJ, 192, L37
De Lucia, F. C., Helminger, P., & Gordy, W. 1971, Phys. Rev. A, 3, 1849
Dotson, J. L., Vaillancourt, J. E., Kirby, L., Dowell, C. D., Hilderbrand, R. H., & Davidson, J. A. 2010, ApJS, 186, 406
Gardner, F. F., & Boes, F. 1987, PASA, 7, 185
Gardner, F. F., & Whiteoak, J. B. 1981, MNRAS, 194, 37
Goldsmith, P. F., Bergin, E. A., & Lis, D. C. 1997, ApJ, 491, 615
Güsten, R., Genzel, M., Wright, M. C. H., Jaffe, D. T., Stutzki, J., & Harris, A. 1987, ApJ, 318, 124
Helmich, F. P., Jansen, D. J., de Graauw, Th., Groesbeck, T. D., & van Dishoeck, E. F. 1994, A&A, 283, 626
Hofner, P., Wyrowski, F., Walmsley, C. M., & Churchwell, E. 1997, ApJ, 536, 393
Hunter, T. R., Brogan, C. L., Indebetouw, R., & Cyganowski, C. J. 2008, ApJ, 680, 1271
Jura, M. 1974, ApJ, 190, L33
Kawabata, K. S., et al. 2010, Nature, 465, 326
Kobayashi, C., Umeda, H., Nomoto, K., Tominaga, N., & Ohkubo, T. 2006, ApJ, 653, 1145
Kuiper, T. B. H., Whiteoak, J. B., Peng, R., Peters, W. L., III., & Reynolds, J. E. 1993, ApJ, 416, L23
Kwan, J., & Scoville, N. Z. 1975, ApJ, 195, L85
Latvakoski, H. M., Stacey, G. J., Gull, G. E., & Hayward, T. L. 1999, ApJ, 511, 761
Leong, M., Peng, R., Houde, M., Yoshida, H., Chamberlin, R. A., & Phillips, T. G. 2006, Proc. SPIE, 6275, 62750P
Lis, D. C., Serabyn, E., Keene, J., Darren, C. D., Benford, D. J., & Phillips, T. G. 1998, ApJ, 509, 299
Lis, D. C., et al. 2010, A&A, in press (arXiv:1007.1461)
Menten, K. M., Wilson, R. W., Leurini, S., & Schilke, P. 2009, ApJ, 692, 47
Morris, M., & Serabyn, E. 1996, ARA&A, 34, 645
Mundy, L. F., Scoville, N. Z., Baath, L. B., Mason, C. R., & Woody, D. P. 1986, ApJ, 304, L51
Neufeld, D. A., & Green, S. 1994, ApJ, 432, 158
Neufeld, D. A., & Wolfire, M. G. 2009, ApJ, 706, 1594
Nomoto, K., Hashimoto, M., Tsujimoto, T., Thielemann, F.-K., Kishimoto, N., Kubo, Y., & Nakasato, N. 1997, Nucl. Phys. A, 616, 79
Nomoto, K., Tominaga, N., Umeda, H., Kobayashi, C., & Maeda, K. 2006, Nucl. Phys. A, 777, 424
Perets, H. B., et al. 2010, Nature, 465, 322
Salez, S., Frerking, M. A., & Langer, W. D. 1996, ApJ, 467, 708
Schilke, P., Phillips, T. G., & Wang, N. 1995, ApJ, 441, 334
Schneider, N., Stutzki, J., Winnewisser, G., & Block, D. 1998, A&A, 335, 1049
Schöier, F. L., Fong, D., Bieging, J. H., Young, K., & Hunter, T. R. 2007, ApJ, 670, 766
Schöier, F. L., & Olofsson, H. 2000, A&A, 359, 586

Schöier, F. L., & Olofsson, H. 2001, A&A, 368, 969
Schöier, F. L., Olofsson, H., & Lundgren, A. A. 2006, A&A, 454, 247
Tafalla, M., Bachiller, R., Wright, M. C. H., & Welch, W. J. 1997, ApJ, 474, 329
Tang, Y.-M., Ho, P. T., Girart, J. M., Rao, R., Koch, P., & Lai, S.-P. 2009, ApJ, 695, 1399
Thompson, M. A., & Macdonald, G. H. 1999, A&AS, 135, 531
Travaglio, C., Hillebrandt, W., Reinecke, M., & Thielemann, F.-K. 2004, A&A, 425, 1029
van der Tak, F. F. S., Black, J. H., Schöier, F. L., Jansen, D. J., & van Dishoeck, E. F. 2007, A&A, 468, 627
van Dishoeck, E. F., Blake, G. A., Jansen, D. J., & Groesbeck, T. D. 1995, ApJ, 447, 760
van Dishoeck, E. F., Jansen, D. J., & Phillips, T. G. 1993, A&A, 279, 541
Whiteoak, J. B., & Peng, R. 1989, MNRAS, 239, 677
Williams, J. P., Mann, R. K., Beaumont, C. N., Swift, J. J., Adams, J. D., & Hora, J. 2009, ApJ, 699, 1300
Wyrowski, F., Heyminck, R., Güsten, R., & Menton, K. M. 2006, A&A, 454, L95
Zhang, Y., Kwok, S., & Dinh-V, T. 2009, ApJ, 691, 1660
Zmuidzinas, J., Blake, G. A., Carlstrom, J., Kneene, J., & Miller, D. 1995, ApJ, 447, L125